International Symposium
On Turbulence and Shear Flow
Phenomena (TSFP-8)
August 28 - 30, 2013 Poitiers, France

CONTROL OF THREE-DIMENSIONAL FLOW OVER A TURRET WITH A FLAT APERTURE

Miguel R. Palaviccini
Mechanical and Aerospace Engineering Department
IMG, University of Florida
Gainesville, FL 32611, USA
mrp1124@ufl.edu

Louis N. Cattafesta III
Department of Mechanical Engineering
FCAAP, Florida State University
Tallahassee, FL 32310, USA
lcattafesta@fsu.edu

ABSTRACT

A study of the baseline flow physics around a submerged hemispherical turret with a flat aperture at Ma < 0.26 is characterized, identifying potential sources of aero-optic distortion. Unsteady pressure measurements reveal that the recirculation region and separated shear layer are two dominant regions contributing to the unsteadiness of the flow. Oil flow-visualization illustrates the three dimensional separation line and length of recirculation region, both investigated as possible metrics for flow control applications. Stereoscopic PIV is used to characterize the separated shear layer showing its two-dimensional nature near the separation location. Malley probe measurements are made along the flat window, providing one-dimensional slices of optical wavefronts in the direction of the beam propagation vector. Passive control is implemented via cylindrical pins to generate streamwise vortices that promote cross stream mixing between the high momentum freestream and the lower momentum boundary layer. Flow visualization determined that the length of the recirculation region shows a direct correlation with the measured aero-optics. Active flow control is achieved via steady blowing along the top portion of the flat aperture. Results suggest that full reattachment along the window is not necessary to achieve an improvement in the optical environment.

INTRODUCTION

When a laser-optical system is mounted within a protuberance on a moving aircraft, the resulting apparatus is termed an aero-optical aircraft turret. It is well known that airborne optical systems are affected by random density fluctuations caused by turbulent flow. As a laser travels through a highly variant index of refraction flow-field, it is subject to refraction by density gradients. This results in the scattering of light and reduction of transmitted laser intensity which is clearly detrimental to the performance of the system. Research has shown that a laser's intensity could be reduced to under 10% of its otherwise ideal performance for an optical turret at flight Mach numbers of as low as 0.7 (Cicchiello & Jumper, 1997). The study of these near-field aberrations is termed the aero-optic problem.

Researchers have focused on using both passive and active open-loop control techniques to suppress aero-optic distortion. Passive control techniques generally use geometric modifications to transfer energy, say from the freestream to the boundary layer, to modify the flow over the aerodynamic body. The control is passive in the sense that no external energy is introduced into the flow, and no sensing or actuation is needed. In open-loop active control, sensors are not used for feedback and the actuation does not depend on any flow parameter. While most of the previous research results are promising, recent investigations have focused on techniques to reduce aero-optic distortion for conformal window turrets. Previous work has shown that turrets with a conformal window present an environment where aero-optical aberrations are consistently lower than those created in a turret with a flat aperture (Gordeyev & Jumper, 2009). Unlike flow control over a conformal window, flow control can likely only move the separation point to the discontinuity associated with the optical flat for a flat aperture turret.

This study therefore examines the effects of both passive and active control to further understand the potential effectiveness of control along with the resulting influences on flow topology around a three-dimensional turret with a flat aperture. First, the experimental set-up is presented. Then, the baseline flow is characterized using surface oil flow visualization, unsteady pressure, stereoscopic particle image velocimetry (sPIV) and aero-optic measurements are introduced. These results help identify potential sources of both flow separation and aero-optic distortion, specifically focusing on the interaction of the various flow features that are present in the low-subsonic flow regime. Once a clear understanding of the baseline flow is established, the main goal shifts toward the evaluation and implementation of flow control. Finally, the results are summarized.

EXPERIMENTAL SETUP

A submerged surface-mounted hemisphere with flat window is used in this study. The coordinate axis and corresponding terminology is shown in Figure 1. The model has a diameter of 231 mm with a slope discontinuity of 42^o between the flat window (110 mm in diameter) and the hemisphere. The model is submerged such that its height protruding from the surface is only 88.9 mm, corresponding to a height to radius ratio of $H/R = 0.77$.

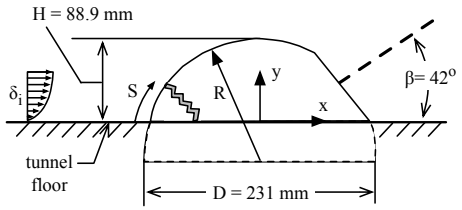

Figure 1. Model dimensions and relevant parameters.

The model is installed in a recirculating type tunnel with a maximum freestream velocity of 90 m/s (corresponding to a maximum $\mathrm{Re}_H = 5.10 \times 10^5$ and Ma $= 0.26$) and the turbulent intensity levels are below 0.1%. The turret model encounters a two-dimensional boundary layer with measured boundary layer parameters: $\delta = 29.5 \pm 3$ mm, $\delta^* = 4.3 \pm 0.2$ mm, $\theta = 3.1 \pm 0.1$ mm. The tunnel blockage imposed by the turret is less than 4%.

Passive Control Model

The purpose of the passive devices is to produce small scale spanwise disturbances to disrupt the coherent nature, and

Table 1. Passive control configurations.

	d/δ=0.6			d/δ=1.2	
Case	s/δ	h/δ	Case	s/δ	h/δ
P1	13.7	6.7	P7	13.7	6.7
P2	6.8	6.7	P8	6.8	6.7
P3	3.4	6.7	P9	3.4	6.7
P4	13.7	0.7	P10	13.7	0.7
P5	6.8	0.7	P11	6.8	0.7
P6	3.4	0.7	P12	3.4	0.7

hence reduce the intensity of the main shear layer. The twelve tested configurations include cylindrical pins that are thicker ($d/\delta > 1$) or thinner ($d/\delta < 1$) and taller ($h/\delta > 1$) or shorter ($h/\delta < 1$) than the boundary layer as measured at the apex of the turret. For all configurations, the spacing between the centers of the pins (s/δ) is also varied. The pins are arranged along the 'chord-wise' centerline ($x = 0$) of the model in several configurations. The geometric parameters and all test cases are presented in Table 1.

Active Control Model

A new turret model is designed and fabricated to allow for steady blowing tangential to the flat window. A slot is comprised of 17 individual orifices oriented such that the flow travels directly down the flat window. Each orifice has a diameter of 2.27 mm and are spaced equidistant from each other (5.25 mm apart) along the upper portion of the window. Pressurized air is provided by a 300 HP Sullari LS20T compressor. An Alicat mass flow controller (MFC), model 2000SLPM, is used to regulate the mass flow. The MFC uses a simple PID controller to keep the flow rate (measured in standard liters per minute, SLPM) fixed at the desired set-point. Multiplying this value by the referenced density (based on 25 C and 101.32 kPa), the true mass flow $\dot{m}$ can be calculated. However, a more useful parameter is the coefficient of momentum,

$$C_\mu = \frac{\dot{m}V_j}{\rho_\infty U_\infty^2 A_0}, \tag{1}$$

where V_j is the mean jet velocity, ρ_∞ is the freestream density, and U_∞ is the freestream velocity. The reference area A_0 is defined as the frontal area of the turret model.

Measurement Techniques

Unsteady surface pressure measurements along the flat window of the model provide a means of measuring the pressure fluctuation footprint left by the separated flow field in the near wake region. Data are acquired at a sampling frequency of 10,240 Hz for 10 seconds and ac coupled at 0.5 Hz. The data are split into 100 blocks of 1024 samples each, resulting in a 10 Hz bin width. The blocks are averaged using a Hanning window with a 75% overlap, resulting in 206 effective averages and a normalized autospectral random uncertainty of 3.9%. All unsteady pressure measurement locations with respect to the turret window are shown in Figure 2. The unsteady pressure spectral density, *PSD*, is then non-dimensionalized by the dynamic pressure to yield a percentage,

$$\frac{P}{q_\infty} = \frac{\sqrt{PSD \times (U_\infty/H)}}{0.5\rho U_\infty^2} \times 100\%. \tag{2}$$

Surface oil flow visualization provides information on the flow topology surrounding the model. A fluorescent dye is applied to the model and the tunnel is brought to the desired speed. Ultraviolet lights are used to visualize the streaklines marked out by the flow on the surface of the model. These resulting streaklines contain information regarding the flow separation, vortical structures, and the size of the recirculation region behind the turret. No transient flow effects are captured in the time that it takes the tunnel to reach full speed. To capture the flow features, two sets of images are taken simultaneously using Nikon Camera Control Pro software. Each camera is set to capture an exposure of 10 sec, f/8.0, and ISO 200.

Stereoscopic particle image velocimetry (sPIV) allows for non-intrusive measurements of the localized velocity in a flow field. A Quantel Laser Evergreen 200 Nd:Yag laser (200 mJ/pulse) is used to produce a laser sheet along the streamwise centerline of the turret. A total of 500 image pairs are processed per case using LaVision DaVis v8.1 software. The vectors are calculated via a four-pass recursive scheme: two passes each of 64×64 and 32×32 pixel interrogation windows each with a 50% overlap 1:1 circular Gaussian weighting function. On each pass, outliers are rejected based on the value of the correlation peak ratio. Additional outliers are then removed in MATLAB by using multivariate outlier detection (MVOD), as described in Griffin *et al.* (2010).

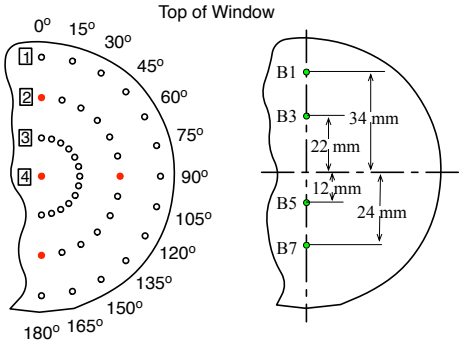

Figure 2. Measurement locations along window for unsteady pressure (left) and Malley probe beams (right). Unsteady pressure locations highlighted by a red marker are used for flow control assessment.

A Malley probe device is used to provide one-dimensional slices of optical wavefronts in the direction of the beam propagation vector. For a general overview of the device, refer to Malley *et al.* (1992). A 10 mW, 532 nm beam is generated with a Coherent CW laser and advances through a beam splitter, generating two parallel beams spaced 10 mm apart. The beams then pass through an optically clear turret window and travel through the turbulent flow created by the wake and separated shear layer. The locations of the beams with respect to the turret window are shown in Figure 2. Once through the flow, the beams are redirected via steering mirrors toward one-inch bi-convex spherical lenses, each with a focal length of 750 mm. The emerging beams are guided to the center of two Newport OBP-A-4L position sensing devices. The spectral density function of the beam deflection angle, $G_{\theta\theta}$, is used to calculated the *rms* optical path difference, OPD_{rms},

$$OPD_{rms} = U_c^2 \int_0^\infty \frac{G_{\theta\theta}}{(2\pi f)^2} df \tag{3}$$

where U_c is the convective speed of aberrating structures. The argument of the estimated frequency response function can then be used to determine the phase lead/lag between the two beam signals. Since the elevation angle β (see Figure 1) and the beam separation distance l are both known, the streamwise convective speed can be calculated, $U_c = (l/sin(\beta))(2\pi\tau)^{-1}$, where τ is the slope of the best line fit to the argument of the estimated frequency response function.

BASELINE FLOW

The baseline flow is first assessed qualitatively using surface oil flow visualization. Figure 3 shows the development of the oil as it travels over the turret at $Re_H = 5.10 \times 10^5$ (Ma $= 0.26$), highlighting some of the key surface features. Upstream of the turret, the incoming boundary layer possesses spanwise vorticity. As the boundary layer encounters the turret, it wraps itself around the turret and creates a horseshoe shaped vortex, giving rise to streamwise vorticity. A stagnation point is formed just upstream of the turret leading edge, and the outer flow is displaced by the turret bluff body. The flow then accelerates along the surface and initially separates along the juncture between the conformal surface and the flat aperture. Along the sides of the turret, the flow continues to stay attached until both three-dimensional effects and an adverse pressure gradient cause the flow to fully separate. Near the junction of the turret

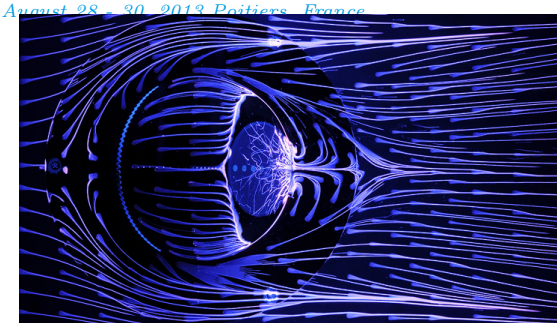

Figure 3. Surface oil flow visualization for the baseline flow at Ma $= 0.26$. Flow is from left to right.

and the supporting wall, however, the boundary stays attached further downstream. The ensuing separated flow creates a recirculating wake that reattaches less than a turret height downstream of the model and causes flow to travel back up the flat window. The horseshoe vortex travels along the spanwise edges of the turret and then separates to continue downstream.

The rear stagnation point is located at $x_R/H = 2.4$ and separates the recirculating region from the downstream flow. This trend is consistent with experiments performed on surface-mounted hemispherical turrets, where the recirculation region spanned approximately a turret diameter away from a trailing edge of the model (Toy *et al.*, 1983). For comparison, turrets mounted on a cylindrical base have much larger recirculation regions, with some cases spanning almost 1.5 turret diameters from the trailing edge of the model (Vukasinovic *et al.*, 2009).

Unsteady surface pressure measurements along the flat window are taken to measure the pressure fluctuation footprint left by the separated flow field in the near wake region. The flat window is rotated about its axis from to 0^o to 180^o, in 15^o increments. To help understand the distribution of unsteady pressure along the window, measured spectra are plotted as surface contours for various frequency ranges. Figure 4 shows the unsteady pressure contour at several frequencies. Each plot shows the third octave band about the listed center frequency, f_c. The lower (f_l) and upper limits (f_h) of the average are calculated by $f_l = f_c/(2^{1/6})$ and $f_h = f_c \times (2^{1/6})$. For the low frequency range shown, ($0.25 < \mathrm{St}_H = fH/U_\infty < 1.0$), the dominant regions of unsteady pressure are concentrated along the portion of the window closest to the base. This is expected, as the main source of unsteady pressure at the low frequencies are the large coherent structures within the recirculation region that manifest their way up from the bottom of the window. For frequencies larger than 1000 Hz ($\mathrm{St}_H > 1.0$), the top-most regions on the window see an increase in unsteady pressure. This is due to the much smaller coherent length scales (high-frequency) embedded within the separated shear layer.

Recall that aero-optic distortion is related to the combination of deflection angle and convective speed (Eq. 3). Therefore, to establish a fair comparison of aero-optic degradation along different window locations, it is important to multiply the beam deflection spectra by the calculated coherent structure speed U_c. Furthermore, to keep the quantity in non-dimensional terms, the spectra is then divided by the freestream velocity U_∞. The deflection angle spectra multiplied by the corresponding convective to freestream speed ratio U_c/U_∞ is shown in Figure 5. Note that only odd beams (B1, B3, B5, and B7) are shown, since the even beams (B2, B4, B6, and B8) are solely used to calculate the convective speed. The magnitude of the normalized beam deflection spectra monotonically increases as the measurement locations are moved closer to the base, indicating that the fluid disturbances have a greater aero-optical effect as they convect downstream. This is due to both the larger shear layer width and higher convective speeds. For the beam closest to the top of the aperture (B1), the broadband peak indicates the presence of the coherent structures within the shear layer (Vukasinovic *et al.*, 2010). As the measurement locations are taken further down the aperture, the peak shifts to lower frequencies which is consistent with the expected shear layer

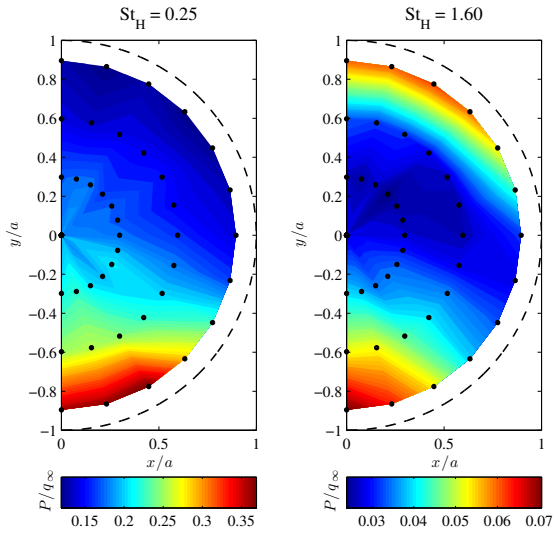

Figure 4. Unsteady pressure contours ($P/q_\infty \times 100\%$) on turret window as a function of frequency (Ma $= 0.26$). Dotted line represents edge of turret window. Sensor locations are shown as black circles. x and y locations along window are normalized by the window radius, a.

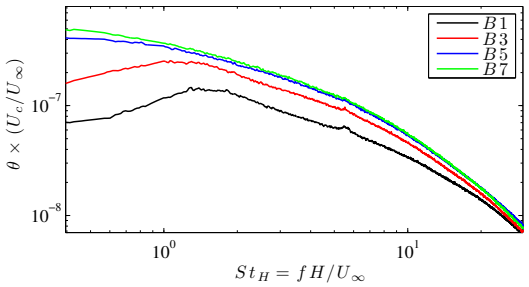

Figure 5. Beam deflection spectra as a function of window location.

growth (and hence larger coherent flow structures).

PASSIVE CONTROL

It is well known that previous flow control techniques have been mainly developed with a need to accommodate the mean aerodynamic requirements (i.e. drag reduction and lift enhancement). However, the metric used to assess control effectiveness becomes more restrictive when flow control is for the purpose of enhancing the transmission of optical wavefronts through regions of highly turbulent flow (Vukasinovic *et al.*, 2009). Since flow separation is due to the abrupt geometric discontinuity associated with the flat window, the introduction of small scale disturbances within the flow to disrupt the formation of coherent structures within the shear layer may be a more viable and attractive flow control option than forced reattachment of the separated flow.

An examination of the calculated OPD_{rms} shows that only P3 is found to improve the aero-optic environment along the entire frequency range of interest. In fact, configuration P9 only reduces the deflection spectra for $1.0 < \mathrm{St}_H < 2.5$ (spectra not shown). This is a relevant find because as technology pushes the bandwidth of fast-steering mirrors, a result like that of P9 may no longer be attractive due to the increase in spectral energy at high frequencies. While cases that reduce the aero-optic aberrations are of primary importance, it may also prove fruitful to study cases that result in a worse optical environment. Configuration P7 falls into this category, providing an increase of OPD_{rms} of 121%. The deflection spectra for this case results in a broadband increase along the entire frequency range.

OPD_{rms} scales by the product of beam deflection angle and convective speed of the aberrating structures ($OPD_{rms} \sim$

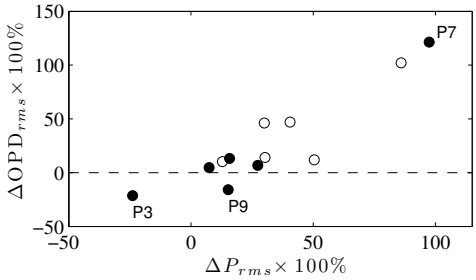

Figure 6. ΔOPD_{rms} as a function of average ΔP_{rms}.

θU_c). Therefore, there are two ways to improve the aero-optic environment: either reduce the beam deflection angle or reduce the convective speed of the problematic structures. An investigation of the constant phase plots reveal that all control cases resulted in a higher convective speed when compared to the baseline. Specifically, configuration P3 an P7 resulted in a convective speed increase from the baseline ($U_c/U_\infty = 0.70$) to $U_c/U_\infty = 1.12$ and 1.01, respectively. This suggests that the primary mechanism for improvement in the flow's optical quality is the diminution of the beam's deflection, and not the decrease in convective speed.

Unsteady pressure was found to correlate well with aero-optic measurements for the baseline flow and can therefore help interpret how the flow unsteadiness ties into aero-optics. To illustrate the correlation between unsteady pressure and aero-optic measurements in a more quantitative manner, Figure 6 plots ΔOPD_{rms} against ΔP_{rms}. The results show a linear trend between the two metrics, suggesting that an increase in one is concomitant with an increase with the other. To determine if there is a linear relationship between the two to standard 95% confidence level, the linear correlation coefficient is calculated. Since the calculated correlation coefficient, $r_{xy} = 0.91$ is larger than the critical correlation coefficient ($\alpha = 0.05$, $n = 12$, $r_t = 0.578$), then there is a linear relationship between ΔP_{rms} and ΔOPD_{rms}, to a 95% confidence level (Wheeler *et al.*, 1996). This encourages the use of unsteady pressure measurements as a feasible metric in real-world applications, where direct aero-optic diagnosis may not be readily available in real time.

To gain further insight into the global flow topology of the controlled flow, oil flow visualization is conducted. Of main interest is the effect of the control on both the separation line and the location of the rear stagnation point, x_R, which defines the extent of the recirculation region.

The effect on separation and recirculation region length for each configuration are studied and there does not seem to be a correlation between the extent of the recirculation region and the location of the separation line with respect to the baseline flow. In general, however, as the spacing between adjacent pins increases, the change in the extent of the recirculation region diminishes. Taking a look at the rear stagnation points of the cases of interest, Figure 7 illustrates that while both passive control cases delay separation, P7 reduces the extent of the recirculation region ($\Delta x_R/H = -5.3\%$) while P3 both widens and extends the length of the recirculation region ($\Delta x_R/H = 27.7\%$). From the oil flow along the aperture (not shown), it is noticeable that the recirculating wake is much stronger in P7 than it is in P3. This results in the energizing of turbulent structures over the aperture, increasing the unsteadiness in near wake region, thereby resulting in an increase in OPD_{rms}.

The general trend between ΔOPD_{rms} and $\Delta x_R/H$ is such that an increase in recirculation region size results in a decrease in the ΔOPD_{rms}. The calculated correlation coefficient, $r_{xy} = -0.51$ is larger than the critical correlation coefficient ($\alpha = 0.10$, $n = 12$, $r_t = 0.497$), so there is a linear relationship between $\Delta x_R/H$ and ΔOPD_{rms}, to a 90% confidence level (Wheeler *et al.*, 1996). These results have significant implications for control of aero-optic distortion, mainly raising the question of using separation control as a metric. The findings instead suggest that the recirculation length may be of more importance. In order to make any firm conclusions, further fluid dynamic measurements – including direct shear layer measurements – need to be assessed and related to the flow visualization findings.

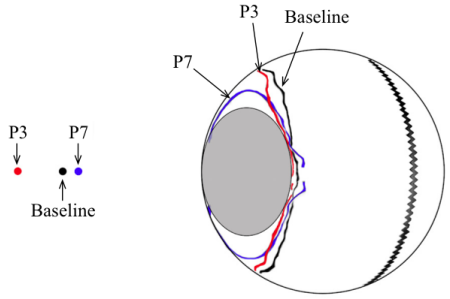

Figure 7. Oil flow visualization for baseline, P3, and P7 cases for Ma=0.26 showing the separation line and the rear stagnation point (x_R) that divides the recirculating region from the downstream flow.

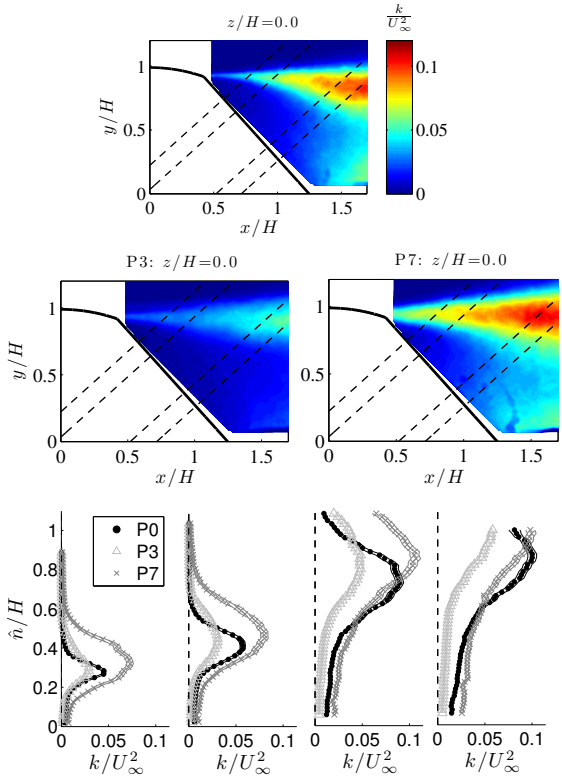

Figure 8. Contour plots of turbulent kinetic energy extracted from sPIV measurements at the center plane ($z/H = 0$). Dotted lines represent beam measurement locations as shown in Figure 2. The bottom plot shows slices of k/U_∞^2 along beam propagation path ($\hat{n}$-direction) of turbulent kinetic energy.

Figure 8 shows the contour of k/U_∞^2 at the center plane ($z/H = 0$). Each beam's propagation path is denoted with dashed lines. Slices of the turbulent kinetic energy are also plotted in Figure 8, with the reference frame transformed such that the data is plotted in the direction normal ($\hat{n}$) to the turret window, i.e. along the beam propagation path. In other words, they show the distribution of velocity fluctuations associated with the path that the beam must travel. The results along the center plane match well with the results from unsteady pressure and recirculation length measurements, showing that configuration P7 results in a wider and more energetic shear layer. By contrast, configuration P3 results in a reduction of the overall turbulent kinetic energy in the shear layer.

Figure 9 plots the ΔOPD_{rms} as a function of $\Delta k/U_\infty^2$ as

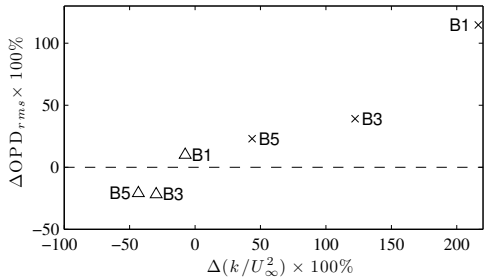

Figure 9. $\Delta\mathrm{OPD}_{rms}$ as a function of average k/U_∞^2 along beam propagation path ($\hat{n}$-direction) for each beam location for P3 ($\triangle$), and P7 ($\times$).

measured along the beam propagation path for pin configurations P3 ($\triangle$) and P7 ($\times$). Note that results from beam location B7 are not included, since the entire measurement domain was not obtained within the sPIV data. The calculated correlation coefficient, $r_{xy} = 0.97$ is larger than the critical correlation coefficient ($\alpha = 0.05$, $n = 12$, $r_t = 0.578$), indicating a linear relationship between $\Delta k/U_\infty^2$ and $\Delta\mathrm{OPD}_{rms}$, to a 95% confidence level (Wheeler *et al.*, 1996).

Since the measurements of turbulent kinetic energy have shown to provide a reasonable indication of optical aberrations within the flow, they can be used to better understand the aero-optic environment along the off-center streamwise planes ($z/H = -0.31$ and -0.62), where Malley probe measurements are not available. The trends are similar along each spanwise plane, with P7 showing an increase in k/U_∞^2 along all beam propagation paths. Again, while the maximum peak intensity isn't affected much for the downstream beam locations, the width of the shear layer increases, causing the beams to travel a longer aberrated path and resulting in an increase in OPD_{rms}. For all cases (baseline and control), the turbulent kinetic energy is reduced as measurement planes move away from the centerline suggesting that control along the centerline is of foremost importance.

ACTIVE CONTROL

For active control, a tangential jet along the upper portion of the turret window is used to force reattachment along the flat window. The means for control stems from the Coanda effect, where the curvature of the model and high speed jet create suction, entraining fluid from the freestream and in turn developing a lateral transport of energy. This induced energy from the freestream enables the flow to overcome the adverse pressure gradient imposed by the window geometric discontinuity allowing the reattachment of the flow over the window. If successful, the resulting flow will be absent of a wake and shear layer, potentially resulting in a more attractive optical environment.

The Malley probe is used to acquire aero-optic measurements at two locations (B3 and B5, as shown in Figure 2) along the flat window. Figure 10 plots $\Delta\mathrm{OPD}_{rms}$ as a function of C_μ for measurement location B3. An increase in steady blowing, up to $C_\mu = 0.21$ causes a direct increase in the measured OPD_{rms}. For larger values of C_μ there is an improvement in the optical environment, with $C_\mu = 0.26$ obtaining the minimum ΔOPD_{rms} (-41%). An increase in steady blowing past $C_\mu = 0.26$ results in. Further increase in steady blowing results in a worsening of the aero-optic environment.

Three cases of interest are chosen for further study: $C_\mu = 0.21$ results in the maximum $\Delta\mathrm{OPD}_{rms}$ (105%), $C_\mu = 0.26$ results in the minimum $\Delta\mathrm{OPD}_{rms}$ (-40.8%), and $C_\mu = 0.38$ results in the minimum $\Delta\theta$ (-41.7%). The deflection angle spectra are plotted for measurement location B3 in Figure 10. For the measurement location B3 (closest to the jet exit) a $C_\mu = 0.21$ results in a broadband increase in the spectra relative to the baseline, most likely due to the addition of energy into the flow without the benefit of flow reattachment. A further increase to $C_\mu = 0.26$ results in the largest decrease in the overall

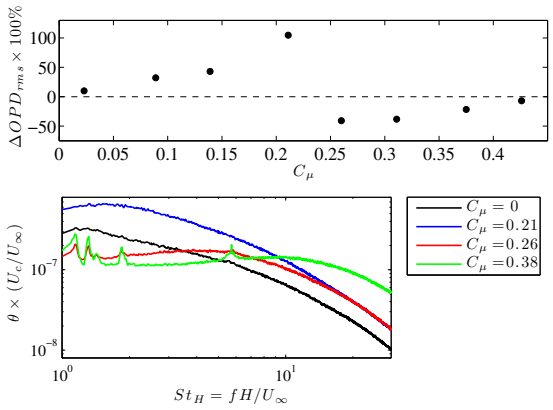

Figure 10. Contour plot of mean velocity for select active control case at all three measurement planes $z/H = 0$.

OPD_{rms}. Most notably, the reduction occurs for $\mathrm{St}_H < 3.5$, indicating that the steady blowing is reattaching the flow over the flat window, resulting in the removal of the large scale structures that were present within the recirculating region in the baseline flow. Finally, for $C_\mu = 0.38$, the spectra values are lower than any other case for $\mathrm{St}_H < 5$, but the addition of extra momentum results in an increase in the calculated deflection spectra at higher frequencies. Similar results are seen further downstream at measurement location B5 (not shown).

The contour plots in Figure 11 show mean three-dimensional velocity along the three measurement planes. Along the symmetry plane ($z/H = 0$), it is clear that for $C_\mu = 0.21$, there is still a small recirculation region, which explains the low-frequency content measured with the Malley probe (Figure 10). With increased blowing to $C_\mu = 0.26$, more ambient fluid is entrained, and the mean flow shows further reattachment along the window. Full reattachment is only achieved for $C_\mu = 0.38$. Along the $z/H = -0.31$ plane, the jet has less of an effect on the separation. All three control cases show a redirection of the mean flow, but none show full reattachment. Note that at this location the slot is further from the baseline separation point, therefore requiring more steady blowing to achieve similar results. Finally, along the edge of the window ($z/H = -0.62$) where there is no longer any slot blowing, the mean velocity profiles are not easily distinguishable. While these finding match the results from flow visualization and provide a better general understanding of the mean flow, they do not provide a clear picture of the aero-optic environment in the near wake region. Instead, the contours of turbulent kinetic energy are used to help elucidate the turbulent flow field.

Figure 12 shows the contours of k/U_∞^2 at symmetry plane, $z/H = 0$. Each beam's propagation path is denoted with dashed lines. Slices of the turbulent kinetic energy are plotted, with the reference frame transformed such that the data is plotted in the direction normal ($\hat{n}$) to the turret window, i.e. along the beam propagation path. Since the measurements of turbulent kinetic energy have shown to provide a reasonable indication of optical aberrations within the flow, the metric $\Delta k/U_\infty$ is calculated along the beam propagation path. The results at beam location B3 along the center plane, match well the Malley probe measurements. Specifically, they show that the overall energy is increased for case $C_\mu = 0.21$ ($\Delta k/U_\infty^2 = 27.6\%$, $\Delta\mathrm{OPD}_{rms} = 104.5\%$) and reduced for cases $C_\mu = 0.26$ ($\Delta k/U_\infty^2 = -81.1\%$, $\Delta\mathrm{OPD}_{rms} = -40.8$) and 0.38 ($\Delta k/U_\infty^2 = -93.1\%$, $\Delta\mathrm{OPD}_{rms} = -21.7\%$). As with the passive control configurations, the correlation coefficient is calculated (plot not shown for brevity). The value, $r_{xy} = 0.91$, is larger than the critical correlation coefficient ($\alpha = 0.05$, $n = 8$, $r_t = 0.707$), indicating a linear relationship between $\Delta k/U_\infty^2$ and $\Delta\mathrm{OPD}_{rms}$, to a 95% confidence level (Wheeler *et al.*, 1996).

CONCLUSIONS

It is well known that unsteady flow caused by the separation over a turret has an adverse effect on aero-optic applications. Understanding the various three-dimensional flow

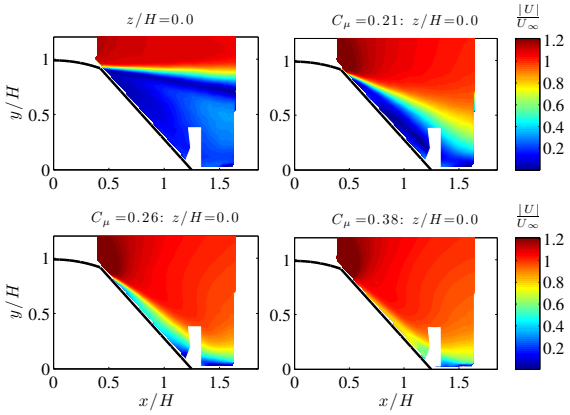

Figure 11. Contour plot of mean velocity for select active control case at all three measurement planes $z/H = 0$.

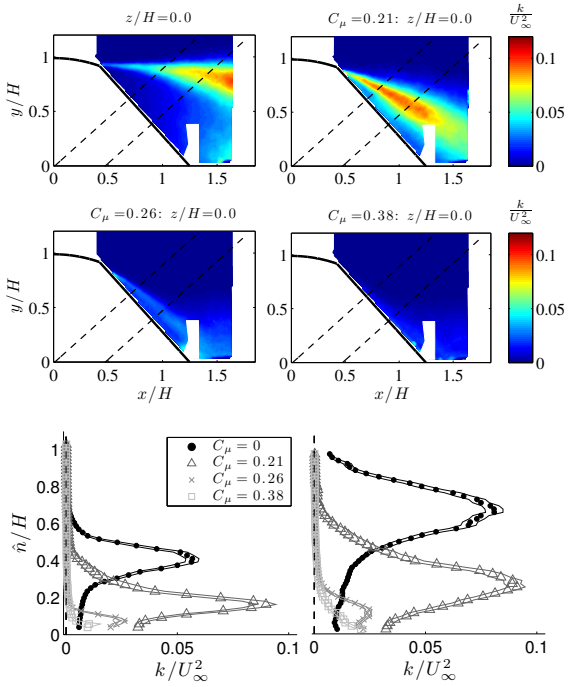

Figure 12. Contour plots of turbulent kinetic energy extracted from sPIV measurements at the center plane ($z/H = 0$). Dotted lines represent beam measurement locations B3 and B5 as shown in Figure 2. The bottom plot shows slices of k/U_∞^2 along beam propagation path ($\hat{n}$-direction) of turbulent kinetic energy for each beam location.

features and their effects on both the fluid dynamics and aero-optics is a key challenge that needed to be addressed. The baseline flow was first characterized and then direct wake control in the form of vortex generating pins was implemented.

Unsteady pressure measurements reveal that both the recirculation near the base of the turret and the separated shear layer contributed to the unsteadiness of the flow. Oil flow visualization results illustrated the separation location along the conformal portion of the turret and the recirculation region along the base of the turret. Aero-optic measurements were made at several locations along the flat window, providing one-dimensional slices of optical wavefronts in the direction of the beam propagation vector. Since this was the first set of experiments that uses a surface-mounted, flat-windowed turret, the calculated OPD_{rms} values are compared to previous work that utilizes other turret model types. When non-dimensionalizing the calculated OPD_{rms} by the suggested scaling, $sin(\alpha)/(2HMa^2)$, the results show that the flow around a surface-mounted, flat-window turret is more than twice as optically active as the flow surrounding a surface-mounted conformal-window turret.

Passive control was implemented by installing cylindrical pins normal to the surface along the streamwise centerline, introducing small scale disturbances that propagate downstream and interact with the separated shear layer. It was found that for all pin configurations, there was a direct correlation between unsteady pressure and the aero-optic environment. Surface oil-flow visualization, determined that for a flat-window turret, separation delay should not be used as a metric when assessing aero-optic distortions. Instead, the length of the recirculation region provided further insight. Finally, direct shear layer measurements showed that the main causes of the increase in OPD_{rms} was tied to both the thickening of the shear layer and increase in maximum turbulent fluctuations. Future work may involve the implementation of an active control strategy that uses unsteady microjets that pierce through the boundary layer and introduce small scale disturbances in a similar fashion to the pins.

Active flow control was implemented using tangential blowing along the upper portion of the turret window, with the main objective being to force reattachment along the flat window. This has the potential to result in a more attractive aero-optical environment by removing both the recirculating wake (in the immediate region behind the window) and highly turbulent shear layer. Calculations of ΔOPD_{rms} show that for steady blowing up to $C_\mu \leq 0.21$, there is a monotonic increase in the deflection spectra. Further blowing results in a decrease in the calculated ΔOPD_{rms}, with the minimum occurring for $C_\mu = 0.26$. This suggests that *there is an optimum amount of steady blowing, with any excess resulting in a degradation of the optical environment*. Then, based on the $C_\mu = 0.26$ case, both flow visualization and mean velocity profiles from sPIV demonstrate that *full reattachment along the window need not be necessary to achieve a reduction in* OPD_{rms}. Furthermore, oil flow visualization shows that significant wake modification is only possible near the centerline of the model, indicating that the location of the slot is too far downstream to reattach the flow along the outer conformal portions of the turret. This gives rise to future work focusing on relocating the slot closer to, and perhaps upstream of, the three-dimensional separation line and perhaps extending it beyond the sides of the window.

REFERENCES

Cicchiello, J.M. & Jumper, E.J. 1997 Far-field optical degradation due to near-field transmission through a turbulent heated jet. *Applied optics* **36** (25), 6441–6452.

Gordeyev, S. & Jumper, E. 2009 Fluid dynamics and aero-optical environment around turrets. AIAA Paper 2009–4224.

Griffin, John, Schultz, Todd, Holman, Ryan, Ukeiley, Lawrence S & Cattafesta, Louis N 2010 Application of multivariate outlier detection to fluid velocity measurements. *Experiments in Fluids* **49** (1), 305–317.

Jumper, E. J. & Fitzgerald, E. J. 2001 Recent advances in aero-optics. *Progress in Aerospace Sciences* **37** (3), 299–339.

Malley, M., Sutton, G. & Kincheloe, N. 1992 Beam-jitter measurements of turbulent aero-optical path differences. *Applied Optics* **31** (22), 4440–4443.

Toy, N., Moss, W.D. & Savory, E. 1983 Wind tunnel studies on a dome in turbulent boundary layers. *Journal of Wind Engineering and Industrial Aerodynamics* **11** (1), 201–212.

Vukasinovic, B., Brzozowski, D. & Glezer, A. 2009 Fluidic control of separation over a hemispherical turret. *AIAA J.* **47** (9), 2212–2222.

Vukasinovic, B., Glezer, A., Gordeyev, S., Jumper, E. & Kibens, V. 2010 Fluidic control of a turret wake: Aerodynamic and aero-optical effects. *AIAA J.* **48** (8), 1686–1699.

Wheeler, Anthony J, Ganji, Ahmad Reza, Krishnan, Vaidyanadhan Venkata & Thurow, Brian S 1996 *Introduction to engineering experimentation*. Prentice Hall Englewood Cliffs, NJ.